J Bionic Eng 17 (2020) 523–538
DOI: https://doi.org/10.1007/s42235-020-0042-3

Journal of Bionic Engineering
http://www.springer.com/journal/42235

Design, Modeling and Experimentation of a Biomimetic Wall-climbing Robot for Multiple Surfaces

Jinfu Liu[1,2], Linsen Xu[1,3*], Jiajun Xu[2], Tao Li[1], Shouqi Chen[2], Hong Xu[2], Gaoxin Cheng[2], Marco Ceccarelli[4]

1. *Institute of Advanced Manufacturing Technology*, *Hefei Institutes of Physical Science*, *CAS*, *Changzhou* 213164, *China*
2. *Department of Precision Machinery and Precision Instrumentation*, *University of Science and Technology of China*, *Hefei* 230026, *China*
3. *Anhui Province Key Laboratory of Biomimetic Sensing and Advanced Robot Technology*, *Hefei* 230026, *China*
4. *Department of Industrial Engineering*, *University of Rome Tor Vergata*, *Via del Politecnico* 1,00133, *Roma*, *Italy*

Abstract

Wall-climbing robots can work on steep terrain and obtain environment information in three dimensions for human in real time, which can improve operation efficiency. However, traditional single-mode robots cannot ensure the stable attachment on complex wall surfaces. Inspired by the structure characteristics of flies and clingfishes, three bionic structures including the flexible spine wheel, the adhesive material and the adsorption system are proposed. Aiming at task requirements on multiple walls and based on the above three bionic structures, a wall-climbing robot with the composed mode of "grabbing+adhesion+adsorption" is presented *via* the law of mechanism configuration synthesis. Using static analysis, the safe attachment conditions for the robot on smooth and rough walls are that the adsorption force is 30 N or more. Based on Newton's Euler and Lagrange formulas, the dynamic equations of the robot on vertical walls are established to deduce that the maximum theoretical torque of the driving motor is 1.43 N·m at a uniform speed. Finally, the prototype of the wall-climbing robot is manufactured and tested on the vertical lime wall, coarse sandpaper wall and acrylic ceiling wall. Meanwhile, experiment results imply that the average maximum moving speed and the corresponding load are 7.19 $cm \cdot s^{-1}$ and 0.8 kg on the vertical lime wall, 7.78 $cm \cdot s^{-1}$ and 0.6 kg on the coarse sandpaper wall, and 5.93 $cm \cdot s^{-1}$ and 0.2 kg on the acrylic ceiling wall respectively. These findings could provide practical reference for the robot's application on walls.

Keywords: wall-climbing robot, spine wheel, adhesive material, adsorption system

1 Introduction

The wall-climbing robot is an essential branch of robotics due to the operating demand of steep three-dimensional environment including the wall cleaning for tall building, health monitoring for large hydraulic projects and information collecting for military missions[1–4]. However, the application of wall-climbing robots is still confined to special region because of their attachment abilities[5,6]. For example, the wall-climbing robot with magnetic wheels can only be used in special wall surfaces with strong magnetic permeability. Wall-climbing robots with vacuum suction cup can only be applied to smooth wall surfaces. Bionic robots employ biomimetic adhesive materials or spines can only climb alone on smooth or rough surfaces respectively, which are easily affected by wall dust and surface particle sizes. Aiming at task requirements on multiple walls and considering the disadvantages of the above single-mode robots, a wall-climbing robot with the composed mode of "grabbing + adhesion + adsorption" is proposed.

Adsorption method, which is one of the key technologies of the wall-climbing robot, has some adsorption manners including negative pressure adsorption, magnetic adsorption and other methods[7]. Among them, negative pressure adsorption usually uses vacuum pumps to provide adsorption force, which has some advantages including higher stability, stronger adaptability and more reliable structure than the others[8]. Nevertheless, negative press adsorption has an obvious drawback that the vacuum level in seal cage is relatively low, so it often requires a larger airflow and the close contact with the wall[9], which will cause some problems

***Corresponding author:** Linsen Xu
E-mail: lsxu@iamt.ac.cn

containing large noise and over-obstacle capacity. In order to solve these problems, Hillenrand divided the sucker into several chambers which can be controlled by solenoidvalve depending on the internal negative pressure[10,11]. Zhao *et al*. have developed a wall-climbing robot with a flexible inflatable sealing ring placed between the vacuum adsorption unit and wall, which could fit well with the rough wall and reduce the air leakage in the vacuum chamber[12]. Illingworth and Reinfeld proposed a new adsorption structure named the vortex attractor, which can exhaust air from enclosed spaces in real time to keep the negative pressure constant[13].

In view of the characteristics of the flexible joints of insect feet, researchers have proposed a variety of bionic robots and some new biomimetic grabbing methods. The robot with the feet made of the arrays of miniature spines can move on rough walls by interlocking force between wall particles and spines, which have been verified on the robot-Spinybot[14,15]. Another spiny feet has also been used in the robot named RiSE, which have six or four flexible legs adaptable to the scansorial environment[16,17]. Bartsch *et al*. have designed a hexapod climbing robot named Space-Climber, which could climb on relative complicated environment based on bionics methods[18]. With a sharp clawed toe, Chen *et al*. proposed a rough wall-oriented climbing robot pinching into the coarse wall surface to form the gripping force[19]. Using the Full-Goldman template, a two-legged climbing robot named Dyno-Climber has been developed, which can move on the vertical walls at a speed of 67 $cm \cdot s^{-1}$[20]. DROP is the first robot utilizing micro-spine technology from a linear array to a rotary collocation, which has improved the transition ability with simpler body mechanism[21].

Inspired by amazing adhesive abilities of geckos on the horizontal, vertical and inverted smooth surfaces[22], some types of synthetic dry adhesive material have been developed for wall-climbing robots. Yu *et al*. designed a novel legged gecko robots with 16 active DOF and 12 passive DOF, which could climb omni-directional surfaces using dry adhesive material by diagonal gait motion[23]. The robot named Tankbot utilizes the synthetic dry adhesive made of the sticky foam, which can go over obstacles up to 16 mm in diameter[24,25]. The robot named Waalbot can only move up and down on vertical walls by three-feet wheels made of the gecko-inspired fibrillar adhesive footpads[26].

The organization of the paper is given as: Section **1** elucidates biomimetic mechanism. Section **2** proposes thebionic mechanical design. Section **3** and section **4** present the force analysis on the rough and smooth walls respectively. Section **5** describes wall-climbing experiments, and conclusions are shown in section **6**.

2 Biomimetic mechanism

A fly's foot is made up of many irregular micro-spines and two flexible adhesive pads. Figs. 1a and 1b show the foot structure of a fly[27]. As a fly climbs on the rough wall, the locking force is formed by the interaction between the micro-spines or claws and the convex points of the wall instead of penetrating into the wall. The spine tip looks like some tiny needles. Equipped with the structure, flies can steadily grab the asperities on the rough wall. While climbing on the smooth wall, the fly's micro-spines and claws will have no attachment points, since the radius of small convex points on the wall surface is smaller than the radius of micro-spines and claws. However, they seem not to affect the movement performance of flies as what we observe, even when the flies climbs fast on the smooth wall surface. The root cause is that flies use pulvilli forming adhesion force to stick to smooth wall surfaces. The movement way of flies is similar to other hexapods using triangular motion gait, at which the moving speed is slower than the wheeled one. Therefore, we only imitate the characteristics of a fly's spines and pulvilli rather than the whole movement mechanism.

Clingfish has a suction cup consisting of a pelvic fin and some ruga on its abdomen, as shown in Fig. 1c. It can realize the adsorption on rough walls with a roughness ranging from 15 μm to 269 μm. A negative pressure of 0.2 bar – 0.5 bar lower than atmospheric pressure can be generated in the suction cup, which can support 80 – 230 times its own weight. The main reason is that the edge of the flexible suction cup and the wall of the fish are interlaced, which results in great friction and sealing effect preventing effectively the outside air from entering the suction cup. By referring to the adsorption structure, it can be used in the design of robot adsorption system[28].

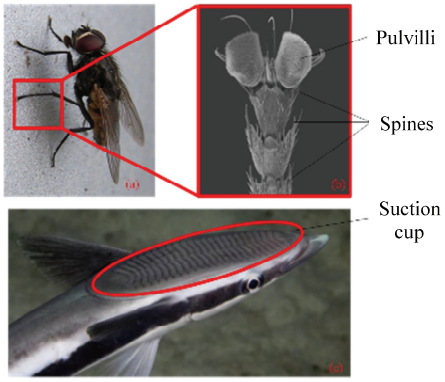

Fig. 1 Morphological features of a fly and clingfish. (a) The climbing state of a fly on the wall; (b) the microscopic structure of the fly foot[27]; (c) the structural features of suction cup of a clingfish[28].

3 Bionic mechanical design

3.1 Spine wheel

According to the feet characteristics of flies, it can be seen that the smaller the diameter of the spine, the easier it is to grasp the wall surface. However, when the diameter of the spine is too small, it will cause the support rod to bend and fail to grasp. Therefore, the stiffness selection is a key factor in the design of the flexible spine wheel. Each supporting rod of a spine is equivalent to a spring whose stiffness is defined as k. During climbing, the deflections of supporting sheet can be modeled by using a 3 × 3 stiffness matrix $\boldsymbol{K}$, which includes the linear stiffness (k_{xx}, k_{xy}, k_{yx}, k_{yy}) and rotational stiffness ($k_{x\delta}$, $k_{y\delta}$, $k_{\delta x}$, $k_{\delta y}$, $k_{\delta\delta}$).

$$\boldsymbol{K}=\begin{pmatrix} k_{xx} & k_{xy} & k_{x\delta} \\ k_{yx} & k_{yy} & k_{y\delta} \\ k_{\delta x} & k_{\delta y} & k_{\delta\delta} \end{pmatrix}. \tag{1}$$

The coordinate system is established in the spine tip, shown in Fig. 2, where x is normal to the wall, y is along the wall and δ is the rotation angle whose counterclockwise direction is positive.

Assuming that the deformation of the spine tip is Δx and the center of rotation is fixed, then the deformation Δl of the supporting rod can be concluded as Eq. (2):

$$\Delta l = l_s - \sqrt{{l_a}^2 + (l_n+\Delta x)^2 - 2l_a(l_n+\Delta x)\frac{{l_n}^2 - l_n l_s\cos\beta}{l_n l_a}}, \tag{2}$$

where l_s is the original length of the supporting rod, l_a is the distance between the spine tip and the wheel hub, l_n is the length of the spine, and β is the original angle between the spine and the supporting rod.

$F_{x,\Delta x}$ is the normal force along x axis, and it can be given as Eq. (3).

$F_{y,\Delta x}$ is the tangential force along y axis, and it can be described as:

$$F_{y,\Delta x} = -\sqrt{(k\Delta l)^2 - \left(F_{x,\Delta x}\right)^2}. \tag{4}$$

$M_{\Delta x}$ is the moment of elastic force versus the contact point between the spine tip and wall, and it can be expressed as:

$$M_{\Delta x} = F_{y,\Delta x}\left(l_n+\Delta x\right). \tag{5}$$

Selecting smaller normal displacement Δx, the element of stiffness matrix $\boldsymbol{K}$ can be obtained as:

$$\begin{cases} k_{xx} = \dfrac{F_{x,\Delta x}}{\Delta x} \\ k_{yx} = \dfrac{F_{y,\Delta x}}{\Delta x} \\ k_{\delta x} = \dfrac{M_{\Delta x}}{\Delta x} \end{cases}. \tag{6}$$

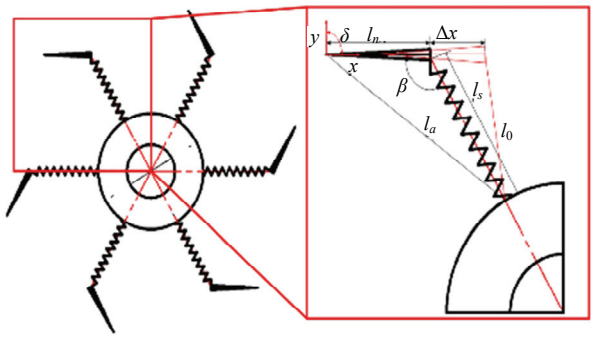

Fig. 2 Schematic diagram when the spine deforms to Δx in x-y plane.

$$F_{x,\Delta x} = -k\Delta l\frac{{l_a}^2 + (l_n+\Delta x)^2 - 2l_a(l_n+\Delta x)\dfrac{{l_n}^2 - l_n l_s\cos\beta}{l_n l_a} + (l_n+\Delta x)^2 - {l_a}^2}{2(l_n+\Delta x)\sqrt{{l_a}^2 + (l_n+\Delta x)^2 - 2l_a(l_n+\Delta x)\dfrac{{l_n}^2 - l_n l_s\cos\beta}{l_n l_a}}}. \tag{3}$$

Similarly, assuming that the tangential and angle deformation of spine tip are Δy and $\Delta\delta$ respectively, the remaining elements of stiffness matrix $\boldsymbol{K}$ can be obtained as:

$$\begin{cases} k_{xy} = \dfrac{F_{x,\Delta y}}{\Delta y} \\ k_{yy} = \dfrac{F_{y,\Delta y}}{\Delta y}, \\ k_{\delta y} = \dfrac{M_{\Delta y}}{\Delta y} \end{cases} \tag{7}$$

$$\begin{cases} k_{xy} = \dfrac{F_{x,\Delta y}}{\Delta y} \\ k_{yy} = \dfrac{F_{y,\Delta y}}{\Delta y}, \\ k_{\delta y} = \dfrac{M_{\Delta y}}{\Delta y} \end{cases} \tag{8}$$

where $F_{x,\Delta y}$ and $F_{x,\Delta\delta}$ are the normal force, and $F_{y,\Delta y}$ and $F_{y,\Delta\delta}$ are the tangential force, and $M_{\Delta y}$ and $M_{\Delta\delta}$ are the of elastic forces versus the contact point when the tangential and angle deformations of spine tip are Δy and $\Delta\delta$ respectively.

According to the known condition in Table 1, independently setting the displacement loads as (1 mm, 0, 0°)′, (0, 1 mm, 0°)′ and (0, 0, 1°)′ in Eq. (1), then the initial stiffness matrix can be obtained as:

$$\boldsymbol{K} = \begin{bmatrix} 0.16k & -0.42k & -1.70k \\ -0.39k & 0.78k & 2.98k \\ -1.88k & -3.54k & 11.92k \end{bmatrix}. \tag{9}$$

Assuming that n spines are distributed uniformly on wheel hub, the angle ξ of adjacent spines is $2\pi/n$. The contact mechanical model between multi-spines and wall surface is shown in Fig. 3. Based on matrix transform theory in different coordinates, the stiffness matrix $\boldsymbol{K}_i$ of the spine i can be described as $\boldsymbol{K}_i = \boldsymbol{T}_i^T \boldsymbol{K} \boldsymbol{T}_i$, where $\boldsymbol{T}_i$ is the transform matrix which can be described as:

$$\boldsymbol{T}_i = \begin{bmatrix} \cos(i\xi) & -\sin(i\xi) & 0 \\ \sin(i\xi) & \cos(i\xi) & 0 \\ 0 & 0 & 1 \end{bmatrix}. \tag{10}$$

$\boldsymbol{F}_i$ is the force acting on the spine i, which can be deduced by the relation of transform matrix $\boldsymbol{T}_i$ and generalized deformation Δr occurring at the spine tip.

$$\boldsymbol{F}_i = \boldsymbol{T}_i \boldsymbol{K} \Delta \boldsymbol{r}. \tag{11}$$

Note that $\boldsymbol{F}_i$ and $\Delta \boldsymbol{r}$ can be expressed as:

$$\begin{cases} \boldsymbol{F}_i = \begin{pmatrix} F_{ix} \\ F_{iy} \\ M_i \end{pmatrix} \\ \Delta \boldsymbol{r} = \begin{pmatrix} \Delta x_i \\ \Delta y_i \\ \Delta \delta_i \end{pmatrix} \end{cases}, \tag{12}$$

where F_{ix} is the normal force perpendicular to wall, F_{iy} is the tangential force along wall, M_i is the moment of wall to the spine tip.

The deformations Δx_i, Δy_i and $\Delta\delta_i$ of the spine i in x, y and δ direction are as:

$$\Delta x_i = x_i = R\sin(i\xi + \beta_o) - R\sin\beta_o, \tag{13}$$

$$\begin{aligned} \Delta y_i = {} & R\frac{\sin(i\xi)}{\sin(i\xi + \beta_o)} \\ & - R\cos(i\xi + \beta_o)\left(1 - \frac{\sin\beta_o}{\sin(i\xi + \beta_o)}\right) - id, \end{aligned} \tag{14}$$

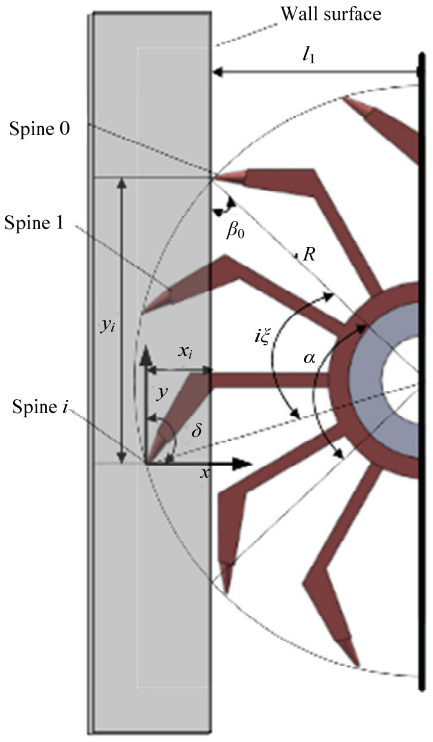

Fig. 3 Contact mechanical model between multi-spines and wall surface.

where R is the distance between the tip of spine 0 and the center of the wheel hub, β_o is the initial contact angle, $i\xi$ is the angle between the line connecting the tip of spine i to the wheeled center and the line connecting the tip of the spine 0 to the wheeled center, and d is the distance of adjacent spines along y axis after spines contacting with wall. Beyond that the value of $\Delta\delta_i$ is 0 due to no rotation between the spine tip and wall.

According to the geometric relationship between spines and wall surface, the maximal number m of spines attaching to wall surface at the same time can be obtained as:

$$m \le \frac{180^\circ - 2\arcsin\frac{l_1}{R}}{\xi}, \tag{15}$$

where l_1 is the distance between the wheel hub and wall surface. According to the known condition in Table 1, we can deduce that the number m of spines contacting with wall surface is 6 at the same time.

Substituting Eqs. (12) – (15) into Eq. (11), the simulation results of F_{ix} and F_{iy} of each spine contacting with the wall can be shown in Fig. 4. In the initial contact with the wall surface, the tangential and normal forces of the spine first rose to a certain value and then gradually decreased to 0, indicating that the spine is exerted a large reverse impact force, which converts into elastic potential energy due to the elasticity of the supporting rod. Therefore, the stage can be defined as the pre-grabbing stage. The forces on the third to fifth spines gradually increases, indicating that as the spine wheel rotate, the elastic deformation for the supporting rods of spines also gradually increases. Then, the stage can be defined as the stable grabbing stage. The force on the sixth spine instantly becomes 0, indicating that the spine is completely detached from the wall surface, which can be defined as the desorption stage. In addition, it can be found that as the stiffness coefficient of the spine increases, the tangential and normal forces also gradually increase.

Considering that the spine wheel made by the shape deposition process are prone to deflection and low strength, three types of spines wheels are made of spring steel (k = 1), tension spring (k = 1) and inelastic steel needle are designed respectively, shown in Fig. 5.

In order to verify the theoretical normal and tangential forces of the spine wheel during the motion cycle, a two-degree-of-freedom orthogonal experimental platform is established, as shown in Fig. 6. The experimental platform is modified by a dynamometer produced by Aidebao Co., Ltd., whose pressure gauges in x direction is used to press spine wheels to control the number of spines contacting with the wall surface and measure the normal force. A set of tensile testing devices is designed in the y direction to measure the maximum tangential force. The coarse sandpaper with a size of P36 is selected as the experiment wall surface. The test results of the above three spine wheels are shown in Table 2. We can know that under the same number of spines contacting the wall surface, the tangential and normal forces of the spine wheel whose material is the spring steel, are basically consistent with the theoretical results. While the values of the spine wheel made of tension spring is relatively low, since the directions of spines is easily twisted and deviated from the wall surface during testing, which will cause the spine has no attachment point. Therefore, both the tangential and the normal forces are less than the theoretical value. In addition, the maximum contacting number is 3 for the spine wheel made of steel needle. When the normal pressure is applied to the steel needle spine wheel, the spines cannot be reset after being deformed, so that there

Table 1 Parameters of a spine

l_n	l_s	β	d	ξ	l_1	R
4 mm	9 mm	20°	3 mm	15°	15.7 mm	17.8 mm

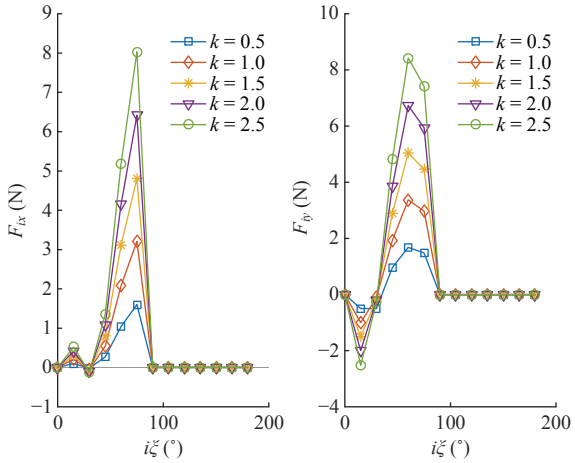

Fig. 4 Forces acting on each spine at different stiffness during a grabbing cycle. (a) The changing trend of the normal force; (b) the changing trend of the tangential force.

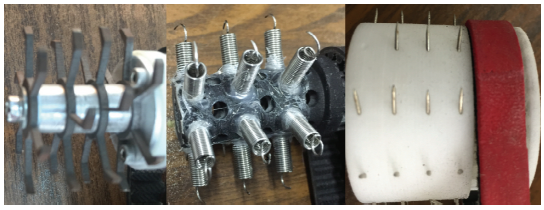

(a) (b) (c)

Fig. 5 Spine wheels. (a) Spine wheel made of spring steel; (b) spine wheel made of tension spring; (c) spine wheel made of steel needle.

are not enough spines to contact the wall surface, which will cause the normal and tangential forces to be relatively small and be prone to wear.

3.2 Adhesive material

The manufacturing steps of adhesive material are shown in Fig. 7. Firstly, wash the silicon wafer with alcohol, acetone, hydrogen peroxide, and concentrated sulfuric acid in order. After soaking for 8 hours, put the silicon wafer in a mixed solution of deionized water, silver nitrate, and hydrofluoric acid. Then soaking for two hours, use deionized water and hydrogen peroxide. Next put the silicon wafer into the mixed liquid of deionized water, hydrogen peroxide, and hydrofluoric acid again to etch the silicon wafer for 480 s to obtain the array features on the surface. And then soaking the silicon wafer in concentrated nitric acid for 60 s again, we can get the template with array features. The next step is to pour polyurethane liquid onto the surface of the silicon wafer to obtain an adhesive layer. Finally, the adhesive layer is affixed to the surface of the rubber belt, and the required adhesive material is manufactured after heating for 1 hour, as shown in Fig. 8.

Adhesive performance testing equipment is HP-10 series hand-cranked tension and pressure dynamometer

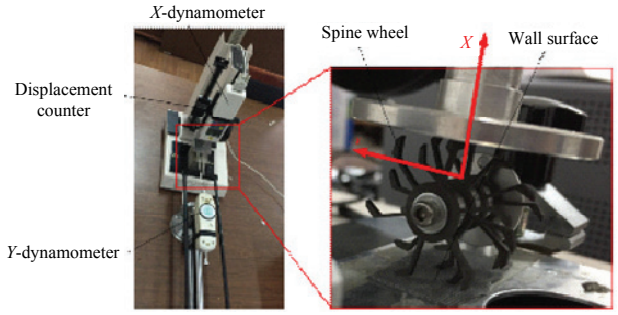

Fig. 6 Experimental testing of normal and tangential forces for three spine wheels.

Table 2 Comparison of normal force and tangential force for three spine wheels

	Pressing distance (mm)	Number of spines contacting with the wall	Tangential force (N)	Normal force (N)
Theoretical value ($k = 1$)	1	1	1.82	2.5
	2	3	4.33	4.5
	3	5	3.85	5.0
	4	6	3.74	5.5
Spine wheel made of spring steel ($k = 1$)	1	1	1.72	2.35
	2	3	4.12	4.36
	3	5	4.26	4.85
	4	6	4.43	5.32
Spine wheel made of tension spring ($k = 1$)	1	1	1.45	1.85
	2	3	2.82	3.24
	3	5	3.74	4.05
	4	6	4.25	4.53
Spine wheel made of spring steel	1	1	2.28	3.25
	2	3	3.32	3.52
	3	3	3.25	3.45
	4	3	3.30	3.43

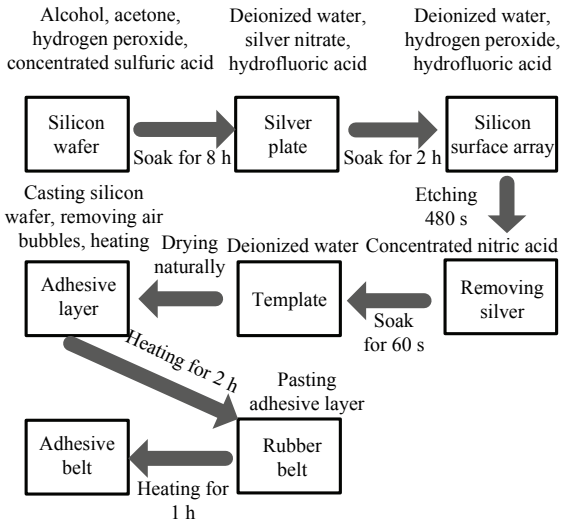

Fig. 7 The manufacturing steps of adhesive material.

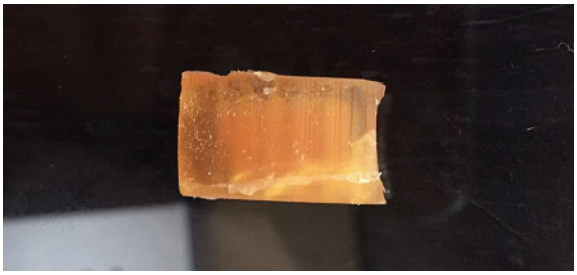

Fig. 8 The adhesive material adhering on glass wall.

made by Aidebao Co., Ltd. as shown in Fig. 9a, whose maximum range load graduation value are 10 N and 0.001 N respectively. The testing equipment consists of a frame, a digital caliper, a dynamometer, an upper clamp, a lower clamp and a hand-cranking device. When testing the tension and pressure of the adhesive material, the adhesive material is fixed on the glass wall. Using the hand wheel to move the supporting rod up and down to achieve the test of samples in different situations, the testing data is converted into electrical signals and transmitted to the computer. The experimental data can be recorded in real time through the testing software, shown in Fig. 9b. The testing mainly includes three following parts: (1) the elastic modulus, (2) change trend of adhesion force versus preload, (3) change trend of tangential force and normal force in different tensile directions. Based on the above experimental data and the Kendall theory, the surface adhesion energy of the material can be derived. The test methods of the adhesive material are shown in Fig. 9c.

In the adhesive theory model of Kendall, it can be known that the peeling force is related to the material elastic modulus which can be obtained with the help of the Hooke's law.

$$E = \frac{\sigma_{\max}}{\varepsilon_{\max}} = \frac{F / A}{\dfrac{\Delta d}{d}}, \tag{16}$$

where $\sigma_{\max}$ is the maximum normal stress, $\varepsilon_{\max}$ is the strain, F is the press force, A is the contact area, Δd is the change in thickness, and d is the thickness of the adhesive material.

The relationship between the pressing force and the thickness change of adhesive material is shown in Fig. 10a. As the deformation of the adhesive material increases, the press force also correspondingly increases, which presents the linear distribution: F=0.115Δd+0.005. The relationship between the elastic modulus and the thickness change is shown in Fig. 10b. It can be known that the elastic modulus fluctuates from 0.055 MPa.

In order to obtain the relationship between the press force and the adhesive force, the force properties of the adhesive material are tested by the indenter at lifting speeds of 2 mm·s^{-1} and 4 mm·s^{-1} respectively, shown in Fig. 11. In the case of lifting speeds of 2 mm·s^{-1}, when the press force is less than 0.7 N, the adhesive force increases linearly. As the press force is greater than 0.7 N, the change of the adhesive force is relatively small, which is basically maintained at about 3.8 N meaning that the stress per unit area is 0.013 MPa. The fitting curve is:

$$y = -6.5x^5 + 29.3x^4 - 45.8x^3 + 26.1x^2 + 0.67x + 0.07.$$

When the lifting speed is 4 mm·s^{-1}, the adhesive force also increases almost linearly. As the press force is less than 0.7 N, the adhesive force value is slightly larger than the one at the lifting speed of 2 mm·s^{-1}. As the press force is greater than 0.7 N, the adhesive force is basically around 4.6 N illustrating that the stress per unit area is 0.015 MPa. The fitting curve is:

$$y = 9x^5 + 41.6x^4 - 66.2x^3 + 38.5x^2 - 0.05x + 0.1.$$

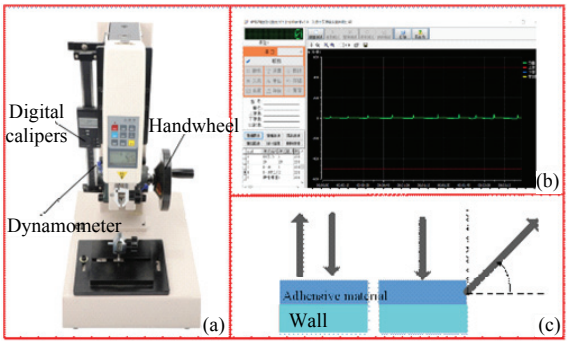

Fig. 9 The performance testing of adhesive material. (a) The testing instrument; (b) the testing software (c) the testing methods.

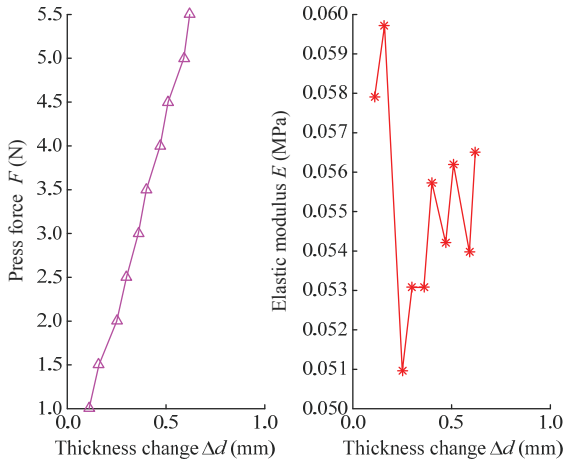

Fig. 10 Testing of the elastic modulus. (a) The relationship between the press force and the thickness change; (b) the relationship between elastic modulus and thickness change.

Setting the press force and the lifting speed to 0.7 N and 2 mm·s^{-1} respectively, the relationship between the maximum peeling force and the peeling angle is tested, as shown in Fig. 12. With the increase of the peeling angle, the peeling force gradually decreases linearly. Since the peeling angle of the adhesive material and the wall is between 60° to 70°, then the required peeling force is about 6 N.

According to the Kendall's peeling theory, the surface energy can be obtained as:

$$\varepsilon = \left(\frac{F}{b}\right)^2 \frac{1}{2dE} + \frac{F}{b}(1-\cos\theta). \tag{17}$$

Substituting the values of elastic modulus, peeling angle, and peeling force, we can obtain the range of the surface adhesion energy is 437.25 J·m^{-2} – 472.25 J·m^{-2}.

3.3 Adsorption system

The structure of adsorption system is shown in Fig. 13, including a vortex fan, a fan frame, a suction cup and a flexible skirt edge. The diameter of the vortex fan is 80 mm, and 8 curved blades are distributed inside. The operating principle is similar to that of the centrifugal pump. The inner air is discharged to form pressure difference through the rotation of the impeller, which ensures that the robot can be attached to the wall surface. The only difference lies in the structure design of the flexible skirt edge composed of wear resistant fabric and elastic adaptive material, which can effectively reduce the external air into the suction cup. When the flexible skirt edge contacts the wall, it will change its shape according to the surface characteristics of the wall to prevent outside air from entering the suction cup.

Due to lower flow rate of air leakage into the suction cup, then the state of the air can be considered as laminar flow. Therefore, using the Navier-Stokes equations, we can obtain:

$$\begin{aligned} f_y - \frac{1}{\rho}\frac{\partial p}{\partial y} + v\left(\frac{\partial^2 v_y}{\partial z^2} + \frac{\partial^2 v_y}{\partial y^2} + \frac{\partial^2 v_y}{\partial x^2}\right) \\ = \frac{\partial v_y}{\partial t} + \frac{\partial v_y}{\partial z}v_z + \frac{\partial v_y}{\partial y}v_y + \frac{\partial v_y}{\partial x}v_x, \end{aligned} \tag{18}$$

where f_y is the mass force in the y direction, ρ is the density of air, p is the pressure in the gap.

Assuming that the gas leakage rate is uniform and not compressible, then we can obtain:

$$\begin{cases} f_x = f_y = f_z = 0 \\ \dfrac{\partial v_x}{\partial x} + \dfrac{\partial v_y}{\partial y} + \dfrac{\partial v_z}{\partial z} = 0 \end{cases}. \tag{19}$$

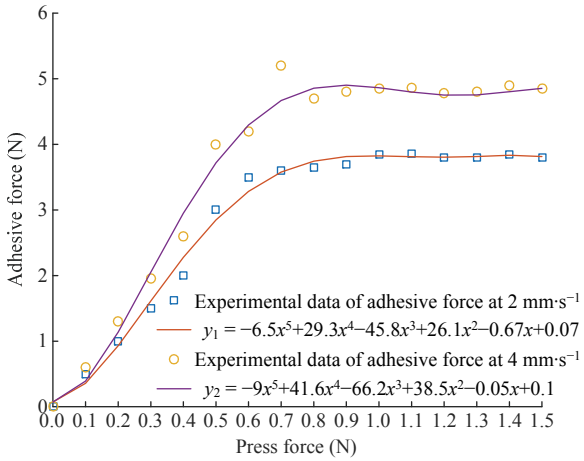

Fig. 11 The relationship between the adhesive force and press force at different lifting speeds.

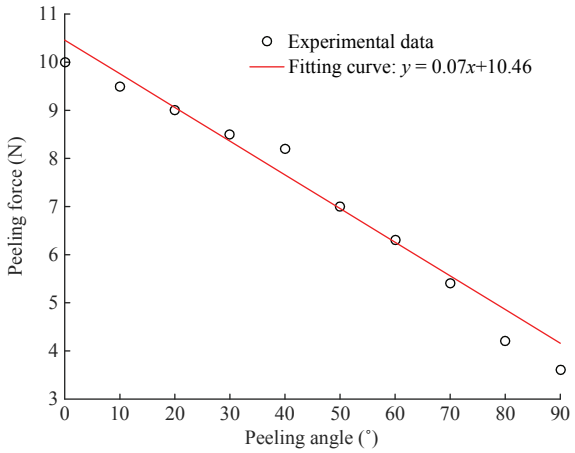

Fig. 12 The relationship between the maximum peeling force and the peeling angle.

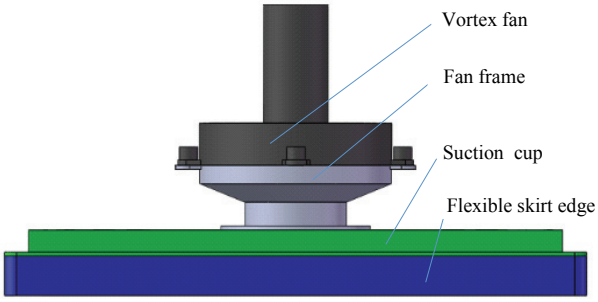

Fig. 13 The virtual prototype model of adsorption system.

Substituting Eq. (19) into Eq. (18), we can deduce

$$\frac{\mathrm{d}^2 v}{\mathrm{d}x^2} = \frac{1}{\mu}\frac{\mathrm{d}p}{\mathrm{d}y}, \tag{20}$$

where v is the velocity of inlet, and μ is the dynamic viscosity.

Integrating Eq. (20) twice and according to the boundary conditions: $x = 0$, $v = 0$. $x = \delta$, $v = 0$. The equation of the flow velocity can be written as:

$$v = \frac{1}{2\mu}x(x-\delta)\frac{\mathrm{d}p}{\mathrm{d}y}. \tag{21}$$

According to Fig. 14, the total air leakage into the suction cup is

$$q = 2\int_0^h v l_1 \mathrm{d}x + 2\int_0^h v l_2 \mathrm{d}x = \frac{h^3}{6\mu a}(p_0 - p_1)(l_1 + l_2), \tag{22}$$

where l_1, l_2 are the length and width of the flexible skirt edge respectively, p_0 is the standard atmospheric pressure, and p_1 is the internal pressure of the suction cup.

Taking a = 10 mm, l_1 = 230 mm, l_2 = 140 mm, the relationship of the air leakage relative to the gap and pressure difference is shown in Fig. 15. When the gap between the skirt edge and the wall is smaller than 0.6 mm, the change range of air leakage is relatively small. However, as the gap is greater than 0.6 mm, the air leakage increases exponentially.

The power required by the fan is:

$$P = (p_0 - p_1)q\rho = \frac{h^3}{6\mu a}(p_0 - p_1)^2(l_1 + l_2)\rho. \tag{23}$$

It can be known from Eq. (23) that the power consumed by the fan is proportional to the cube of the gap, the square of the pressure difference, the air density, and the size of the skirt edge, and inversely proportional to the width of the skirt and air viscosity. The relationship between the power consumption of the fan relative to the gap and the pressure difference can be obtained. As shown in Fig. 16, when the gap is less than 0.6 mm, the power consumed by the fan is relatively small, mainly because the leakage of external air into the sealed cavity is relatively few. When the gap is greater than 0.6 mm, the power required by the fan increases exponentially. In addition, the greater the pressure inside the sealed cavity, the more the power will gradually increase.

The testing equipment of adsorption system is shown in Fig. 17a. The acrylic board and coarse sandpaper with 50 mesh are selected as smooth and rough wall surfaces respectively.

The negative pressure of the suction cup is measured by the pressure sensor (model: SIN-PX300) produced by Hangzhou Meiyi Automation Co., Ltd., whose measurement range is from −50 kPa to 0 kPa. The fan's

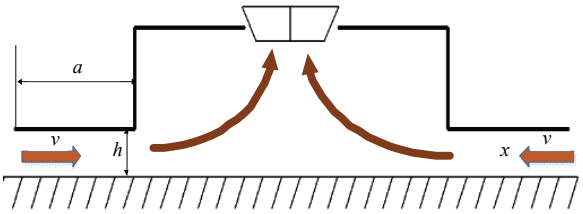

Fig. 14 Fluid model of the suction cup.

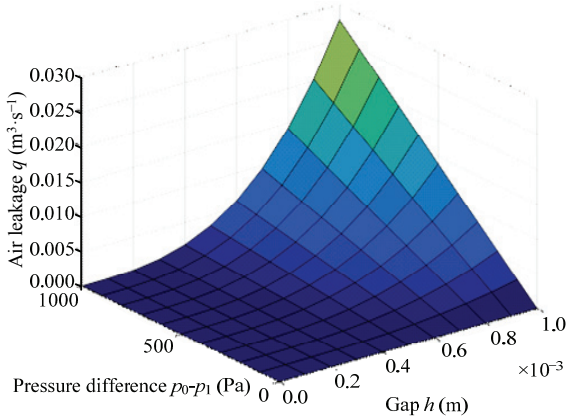

Fig. 15 The relationship of air leakage versus the gap and pressure difference.

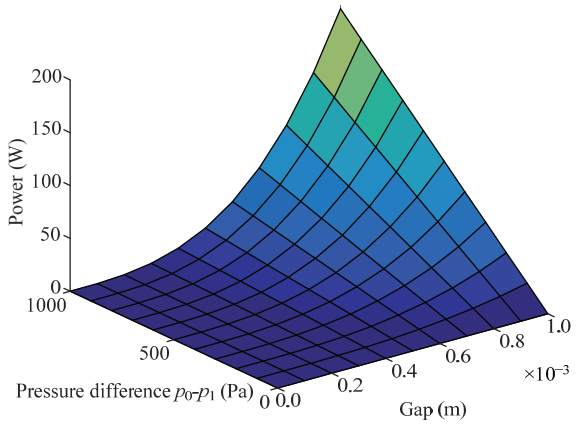

Fig. 16 The relationship of the power versus the gap and pressure difference.

power supply system uses stabilized voltage (model: UTP3305), manufactured by Youdeli Co., Ltd. The gap adjusting device is composed of a hand wheel, a screw and a slider. Connecting the suction cup with the slider, the distance between the skirt edge of the suction cup and the wall can be adjusted by turning the hand wheel. The negative pressure inside the sealed cavity is set to 1000 Pa. Turning the hand wheel to move the suction cup upward by 0.1 mm, then the corresponding ammeter reading is recorded. According to: $P = UI$, the relationship between the power consumption and the gap can be measured indirectly, shown in Fig. 17b. The results show that the experimental value of the power consumption is basically similar to the theoretical one in Fig. 16. Taking the maximum gap of 0.6 mm as an example, the power consumption on the rough wall surface is 15% higher than the one on the smooth wall surface. The main reason is that flow channels have been formed between the particles on the rough wall surface. When the suction cup is separated from the rough wall surface, the actual gap is greater than the one displayed by the vernier caliper, so the air leaking into the sealed cavity will also increase. In order to keep the negative pressure in the vacuum chamber constant, the fan needs to consume more energy to exhaust the internal excess air. The energy consumption of the fan is close to the rated power of the motor 40 W. Therefore, when using the suction cup as the adsorption mechanism of wall climbing robots, the gap should be less than 0.6 mm as much as possible. In addition, the speed of the fan impeller relative to the gap is also tested, shown in Fig. 17. The change of speed is the same as the trend of the energy consumption of the fan. Similarly, taking the maximum gap of 0.6 mm as an example, the speed of the fan on the rough wall is 10.7% higher than the one on the smooth wall.

4 Force analysis of the robot on the rough wall

4.1 Safe attachment conditions

In view of the structural characteristics of the spine wheel, the main forms of failure of the robot on rough walls include the integral sliding and the flipping around the contact point between the rear spine wheels and the wall surface, shown in Fig. 18. The condition that the robot does not slip is that the frictional force in the direction of the wall surface is greater than the component force of gravity. According to the force balance in the tangential and normal direction, we can know:

$$\begin{cases} F_{1f} + F_{2f} \geq G\sin\theta \\ F_{1N} + F_{2N} \geq F_S + G\cos\theta \end{cases}. \tag{24}$$

If the robot does not flip around the contact point between the rear spine wheel and the wall surface, it should be ensured that the front spine wheel cannot be separated from the wall surface, then we can obtain:

$$\begin{cases} F_{1N} + F_{2N2} = F_S + G\cos\theta \\ F_{1N}D + G\sin\theta L_1 - \dfrac{(F_S + G\cos\theta)D}{2} = 0 \end{cases}. \tag{25}$$

According to Eqs. (24) and (25), the minimum adsorption force of the robot on the rough wall surface can be deduced

$$F_S = \max\begin{cases} \dfrac{G\sin\theta}{\mu} - G\cos\theta \\ 2G\sin\theta\dfrac{L_1}{D} - G\cos\theta \end{cases}. \tag{26}$$

Setting the robot's own gravity G = 19.6 N and friction coefficient μ = 0.76, then the relationship between the adsorption force and the slope angle of the wall on the rough wall is shown in Fig. 19. When the slope angle is 50°, the adsorption force gradually becomes positive in the sliding state, indicating that the angle is the critical slipping angle of the robot without a suction cup. When the angle is increased to 70°, the adsorption force in the flipping state gradually becomes positive, illustrating that the angle is the critical flipping angle

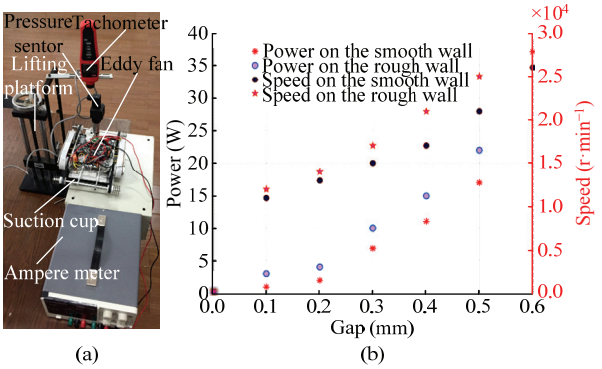

Fig. 17 Adsorption performance testing. (a) Testing equipment, (b) the experimental values of the power and the speed for the fan on smooth and rough wall surfaces.

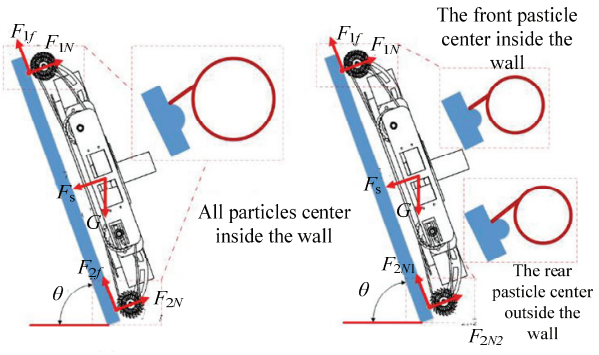

Fig. 18 Safe attachment models on the rough wall surface. (a) Integral slipping model, (b) the flipping model around the contact points between the rear spine wheel and the wall.

without a suction cup. In addition, it can be seen that the minimum adsorption force of the robot on the rough vertical wall is 20 N.

4.2 Dynamic analysis

The force model on the rough wall is shown in Fig. 20, where E is the center of gravity of the robot, F is the center point of the front driving wheels, L_1 is the center distance of the front and rear spine wheels, θ_L is the rotational angle of the left driving wheel, θ_R is the rotational angle of the right driving wheel, r_1 is the radius of the spine wheel, and V_F is the speed at the center of the two front wheels. The dynamic equation can be obtained as:

$$\begin{cases} m\ddot{x}_{\mathrm{E}} + \lambda\sin\varphi = 2\left(F_R + F_L\right)\cos\varphi \\ m\ddot{y}_{\mathrm{E}} - \lambda\cos\varphi = 2\left(F_R + F_L\right)\sin\varphi - G - 2\left(f_R + f_L\right), \\ J_{\mathrm{E}}\ddot{\varphi} - \lambda L_1 = 2\left(F_R - F_L\right)b \end{cases} \quad (27)$$

Eq. (27) can be expressed in the form of Lagrange's equation, as:

$$\boldsymbol{M}(q)\ddot{\boldsymbol{q}} + \boldsymbol{C}(q)F_s + \boldsymbol{D}(q)G = \boldsymbol{B}(q)\boldsymbol{\tau} + \boldsymbol{A}^{\boldsymbol{T}}(q)\lambda, \quad (28)$$

where

$$\boldsymbol{M}(q) = \begin{bmatrix} m & O & 0 \\ 0 & m & 0 \\ 0 & 0 & J_{\mathrm{E}} \end{bmatrix}, \boldsymbol{C}(q) = \begin{bmatrix} 0 \\ \dfrac{\mu}{2} \\ 0 \end{bmatrix}, \boldsymbol{D}(q) = \begin{bmatrix} 0 \\ 1 \\ 0 \end{bmatrix}$$

$$\boldsymbol{A}^{\boldsymbol{T}}(\boldsymbol{q}) = \begin{bmatrix} \sin\varphi \\ -\cos\varphi \\ \dfrac{L_1}{2} \end{bmatrix}$$

5 Force analysis of the robot on the smooth wall

5.1 Safe attachment conditions

On smooth walls, the main forms of instability for the robot are integral slipping, flipping around the contact points between the rear belts and walls, and flipping around the left (or right) adhesive belts, shown in Fig. 21. The conditions under which the robot does not slip are:

$$f = \mu_1 F_{N1} + \mu_2 F_{N2} \geq G\sin\theta. \quad (29)$$

In order to prevent the robot from flipping backward, then $F_{Na} \geq 0$, and the force and moment balance equations of the robot are as:

$$\begin{cases} F_{Na} + F_{Nb} - G\cos\theta - F_S - F_a = 0 \\ G\sin\theta L_1 + F_{Na}L - \left(F_S + F_a + G\cos\theta\right)\dfrac{L}{2} = 0 \end{cases}. \quad (30)$$

The sufficient and necessary condition for the robot's no overturning is that the upper normal support force is not smaller than 0, then we can obtain:

$$\begin{cases} F_{\mathrm{cnf}} + F_{\mathrm{cnb}} = F_{\mathrm{af}} + F_S + F_{ab} + G\cos\theta \\ \left(F_{\mathrm{af}} - F_{\mathrm{cnf}}\right)b + \dfrac{F_S + G\cos\theta}{2}b - G\sin\theta\sin\alpha L_1 = 0 \end{cases}. \quad (31)$$

According to Eqs. (29) – (31), the safe operation conditions of the robot on smooth walls are as:

$$F_S \geq \max\begin{cases} \dfrac{2G\sin\theta}{\mu_1 + \mu_2} - G\cos\theta - F_a \\ 2\dfrac{L_1}{L}G\sin\theta - G\cos\theta \\ 2G\dfrac{L_1}{b}\sin\alpha\sin\theta - 2F_{\mathrm{af}} - G\cos\theta \end{cases}. \quad (32)$$

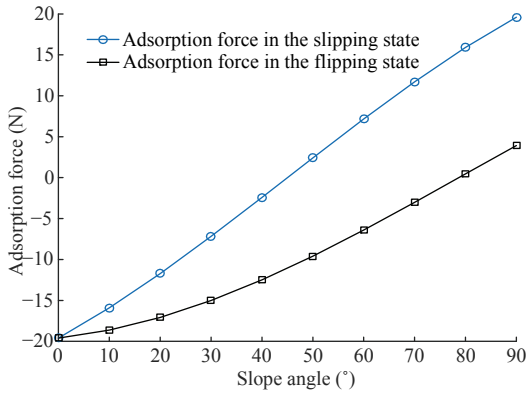

Fig. 19 Variation of the adsorption force relative to the slope angle.

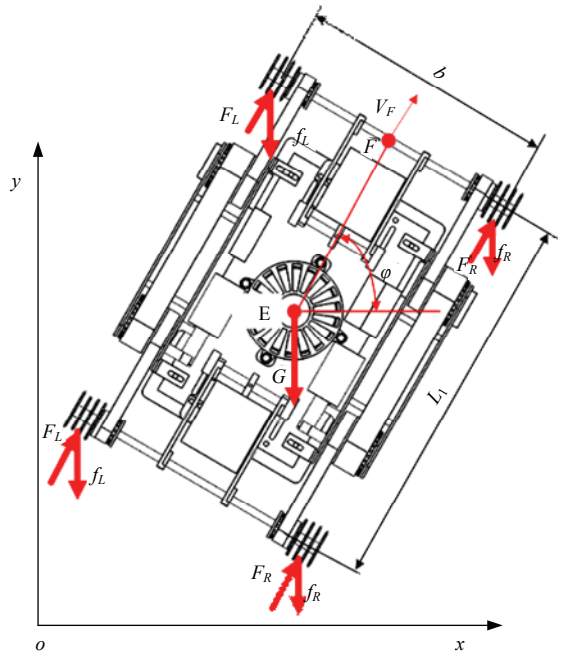

Fig. 20 The mechanical model on the rough wall.

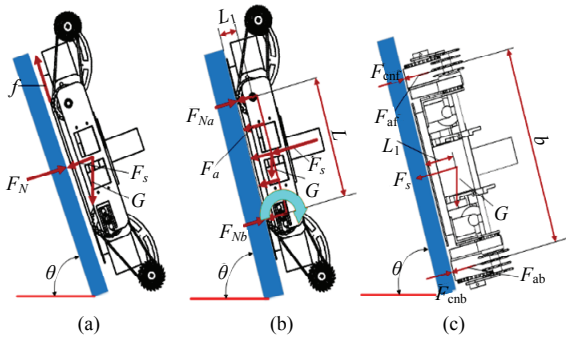

Fig. 21 Safe attachment models on the smooth wall surface. (a) Integral slipping model, (b) the flipping model around the contact points between the rear adhesive belts and the wall, (c) the flipping model around the left (or right) adhesive belts.

Substituting the known parameters: G = 19.6 N, μ_1 = 0.8, μ_2 = 0.5, α = 90°, L_1 = 30 mm, L = 150 mm, b = 200 mm, the simulation of adsorption force can be seen in Fig. 22. When the wall inclination is 90°, the adsorption force reaches up to 30 N, which indicates that the robot is prone to slip at 90°, shown in Fig. 22a. In Fig. 22b, the adsorption force gradually increases as the inclination of the wall surface becomes larger. The maximum adsorption force reaches approximately 22 N at the inclination angle of 180°, indicating that the robot is liable to back flip. In Fig. 22c, the variation trend of adsorption force is similar to the one in Fig. 22b. When the wall inclination angle is 180°, the maximum adsorption force is 18 N, illustrating that the robot occurs easily roll-over. In addition, it can be found that under the same inclination angle of the wall surface, as the adhesive force increases, the adsorption force gradually decreases, since the adhesive belts will share some gravity component of robots. Through a comprehensive analysis for adsorption force in the above three states, in order to ensure that the robot has a safe operating attachment condition, the minimum adsorption force must be greater than 30 N.

5.2 Dynamic analysis

The force model on the smooth wall is shown in Fig. 23. According to the Newton-Euler equation, the dynamic equations of the robot in the coordinate system $x_1o_1y_1$ are expressed as:

$$\begin{cases} m\ddot{x}_1 = -2F_x - G\sin\varphi \\ m\ddot{y}_1 = F_L + F_R - G\cos\varphi - \mu F_s - 2F_P\cos\varphi, \\ I\ddot{\varphi} = (F_R - F_L)\dfrac{b}{2} - 2M_X \end{cases} \quad (33)$$

where m is the mass of the robot, G is the gravity, I is the moment of inertia of the robot around point E, F_P is the peeling force, and φ is the peeling angle of the adhesive belt. Dynamic equations in the coordinate system (xoy) can be expressed as Eq. (34).

Since the robot is only suitable for the up and down movement on vertical walls, both the navigation angle φ and the instantaneous center offset d are 0. Therefore, it

$$\begin{bmatrix} m\ddot{x} \\ m\ddot{y} \\ I\ddot{\varphi} \end{bmatrix} = \begin{bmatrix} \cos\varphi & -\sin\varphi & 0 \\ \sin\varphi & \cos\varphi & 0 \\ 0 & 0 & 1 \end{bmatrix} \begin{bmatrix} -4f_u dB - G\sin\varphi \\ F_L + F_R - G\cos\varphi - \mu F_s - 2F_P\cos\varphi \\ (F_R - F_L)\dfrac{b}{2} - 2f_u B\left(\dfrac{L^2}{4} - d^2\right) \end{bmatrix}. \quad (34)$$

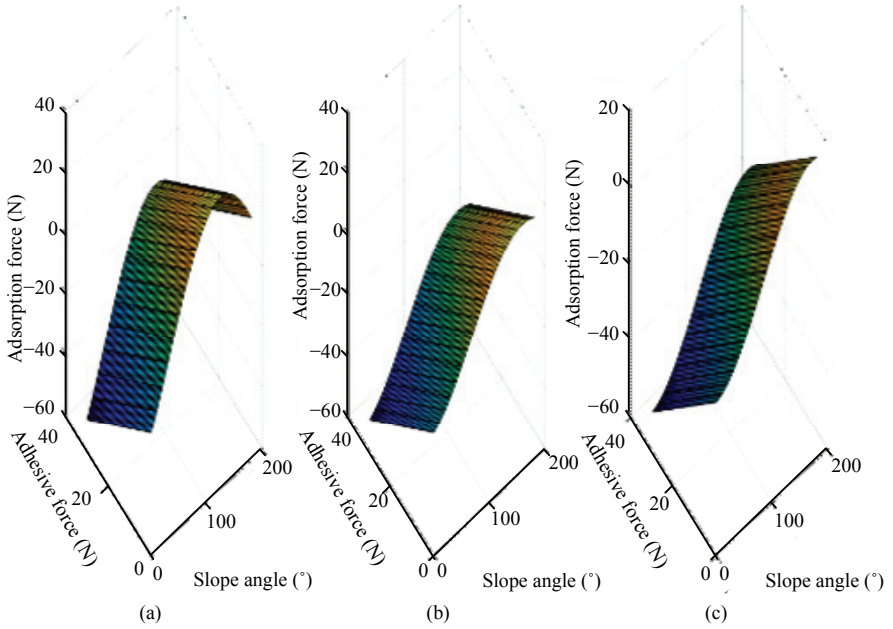

Fig. 22 Simulation of adsorption force relative to the adhesive force and slope angle of wall. (a) Variation of adsorption force during intergral slipping; (b) variation of adsorption force during flipping around the contact points between the rear belts and walls; (c) variation of adsorption force during flipping around the left (or right) adhesive belts.

can be seen that the driving torque is only related to the robot's own gravity, peeling force, peeling angle, adsorption force, and friction coefficient.

6 Wall-climbing experiments

6.1 Mechanism design and dynamic validation

Combining the characteristics of the spine wheel, adhesive material and vacuum adsorption system, a novel multi-mode bio-inspired wall-climbing robot is brought out for various wall surfaces. The robot consists of five parts: the main motion system, the grabbing system, the adhesion system, adsorption system and the control system, shown in Fig. 24. The main motion system includes two brushless DC motors installed on the front of the frame, which can drive the adhesion belts to realize the ascending, descending and turning of the robot. Four spine wheels comprise the grabbing system, which are used to realize the grabbing of particles on the rough wall. The adsorption system contains the vortex fan, suction cup and flexible skirt edge, which can provide the robot with adsorption force during the entire motion cycle. The adhesion system provides the adhesive force to the robot by means of the contact with wall surfaces. The control system includes a control panel and a remote controller to adjust the rotational speeds of

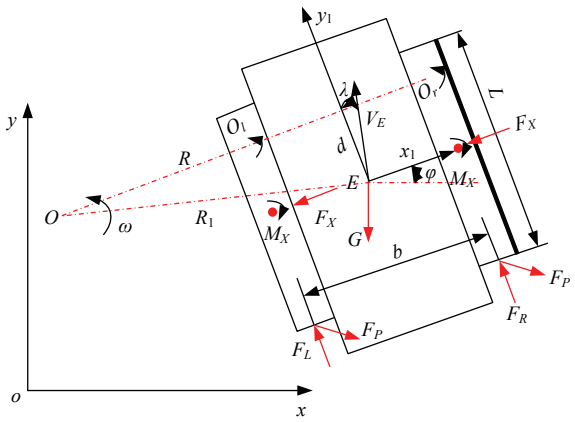

Fig. 23 The mechanical model on the smooth wall.

the vortex fan and the driving motors in real time. The robot has the three-dimensional size 230 mm × 200 mm × 100 mm. In order to meet the requirements of the robot's long-term operation, the key components of the robot must be lightweight. Therefore, the driving and driven wheels are made of nylon using 3D printing technology, and other components such as frame, suction cup housings, fan holders, *etc*., need to bear larger loads, whose material use high-strength aluminum-magnesium alloys. The parameters of the robot are shown in Table 3.

In order to verify the dynamic model of the robot on the smooth and rough wall surfaces, the vertical lime and coarse sandpaper wall surfaces are used as the testing platforms respectively. The torque sensor is produced by Dayang Co. Ltd (model: DYJN-104-3 Nm, range: 3 N·m, accuracy: 1%). Assuming that the robot climbs upwards at a constant moving speed during testing and setting the safety factor to 2, the theoretical and experimental motor torques on the smooth and rough wall surfaces are shown in Fig. 25. According to Eqs. (28) and (34), the theoretical values of the motor driving torque can be deduced as 1.43 N·m and 0.69 N·m respectively. The experimental results show that the testing values basically fluctuate around the theoretical ones. Occasional large fluctuations on the smooth wall are results of the tight attachment between the adhesive belt and the wall, causing that the robot cannot be disengaged instantly. While occasional large fluctuations on the rough wall are caused by the gripping impact owing to inconsistent particles on the wall. Since the maximum fluctuation value on the walls is 1.89 N·m, the rated torque of the motor is selected as 2 N·m. We select the voltage of the motor to 18 V and the radius of the pulley to 1.8 cm, as well as the maximum speed of the robot to 10 $cm \cdot s^{-1}$, and the rated speed of the driving motor is thus derived as 55 $r \cdot min^{-1}$.

6.2 Performance testing

To investigate the wall-climbing performance of the robot on various wall surfaces, the vertical lime wall, the coarse sandpaper wall, and the acrylic ceiling wall are used as testing platforms respectively, as shown in Figs. 26 – 28. The moving speed and load capacity are the important indicators for evaluating the climbing ability of the robot, whose experiment results on the above walls are shown in Table 4. It is can be known that the average maximum moving speed and the corresponding load are 7.19 $cm \cdot s^{-1}$ and 0.8 kg on the vertical lime wall, 7.78 $cm \cdot s^{-1}$ and 0.6 kg on the coarse sandpaper wall, 5.93 $cm \cdot s^{-1}$ and 0.2 kg on the acrylic ceiling wall respectively. Beyond that, it will take 2 s to switch for the robot among the three surfaces. According to the comprehensive analysis for the above experimental results, the robot has the smallest load on the acrylic ceiling wall as a result of the robot's own gravity completely becoming an additional load. On the rough sandpaper wall, the robot does not need to overcome more peeling forces between the adhesive belt and the wall, so it has a relatively fast moving speed. Due to the combined effects of the vacuum adsorption force and the adhesive force on smooth vertical lime wall, then the load is relatively maximum.

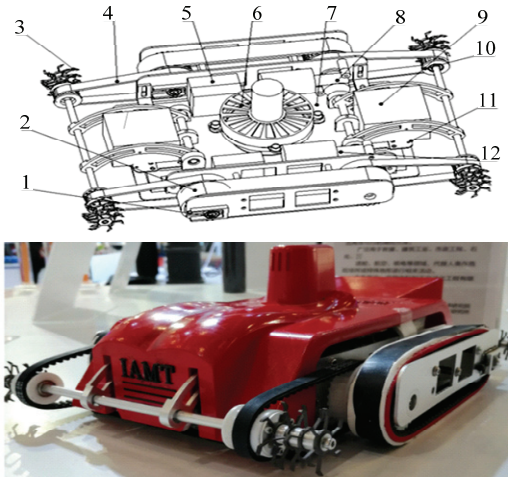

Fig. 24 The principle prototype of the robot. 1-adjustment mechanism; 2-adhesive belt; 3-spine wheel; 4-driving belt; 5-control board; 6-vortex fan; 7-negative press cavity; 8-left driving motor; 9-battery; 10-synchronous pulley; 11-frame; 12-right driving motor.

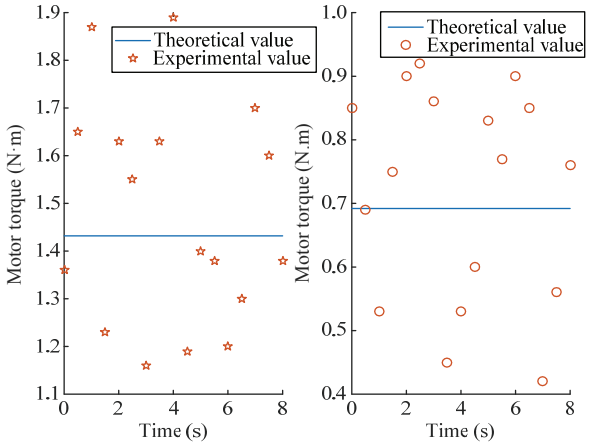

Fig. 25 Motor torque testing. (a) The theoretical and experimental values on the smooth wall, (b) the theoretical and experimental values on the rough wall.

Table 3 The robot specifications

Mass	Length	Width	Height	Climbing angle
2 kg	230 mm	200 mm	100 mm	0° – 360°

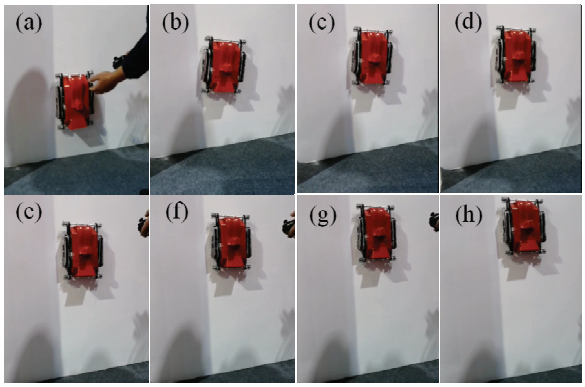

Fig. 26 Still frames from a video showing the principle prototype climbing on the lime surface.

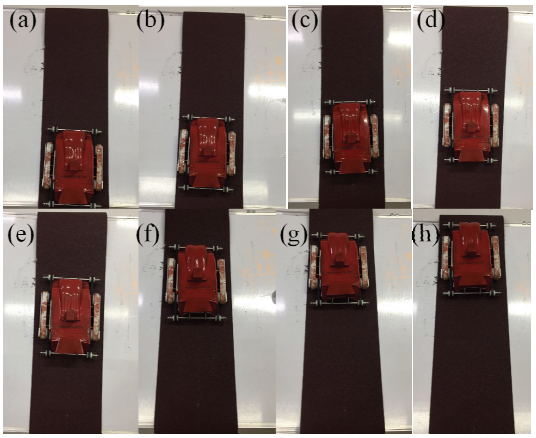

Fig. 27 Still frames from a video showing the principle prototype climbing on the coarse sandpaper surface.

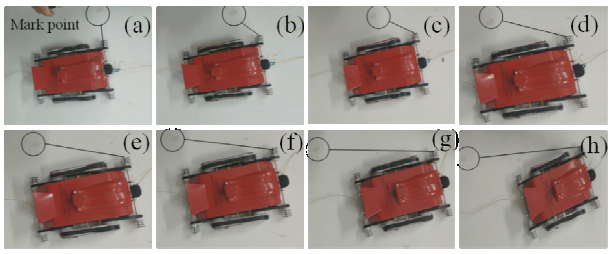

Fig. 28 Still frames from a video showing the principle prototype climbing on acrylic ceiling.

Table 4 The performance testing on the lime, coarse sandpaper and acrylic ceiling wall

Testing number	Lime wall		Coarse sandpaper wall		Acrylic ceiling wall	
	Moving speed ($cm \cdot s^{-1}$)	Load (kg)	Moving speed ($cm \cdot s^{-1}$)	Load (kg)	Moving speed ($cm \cdot s^{-1}$)	Load (kg)
1	7.63	0.8	8.32	0.6	5.86	0.2
2	7.26	0.8	7.56	0.6	6.15	0.2
3	7.05	0.8	7.21	0.6	5.71	0.2
4	6.83	0.8	8.06	0.6	6.35	0.2

7 Conclusion

According to motion principle of flies and clingfishes, three bionic structures including the flexible spine wheel, the adhesive material and the adsorption system have been presented. Using the above three bionic structures, a composed mode wall-climbing robot with "grabbing+adhesion+adsorption" has been represented *via* the law of mechanism configuration synthesis. The safe attachment conditions for the robot on smooth and rough walls are that the adsorption force is 30 N or more by static analysis. Based on Newton's Euler and Lagrange formulas, the dynamic equations of the robot on vertical walls have been established to deduce that the maximum theoretical driving torque of the motor is 1.43 N·m at a uniform speed. Finally, the prototype of the wall-climbing robot has been manufactured and tested on the vertical lime wall, coarse sandpaper wall and the acrylic ceiling wall respectively. Moreover, experiment results indicate that the average maximum moving speed and the corresponding load are 7.19 $cm \cdot s^{-1}$ and 0.8 kg on the vertical lime wall, 7.78 $cm \cdot s^{-1}$ and 0.6 kg on the coarse sandpaper wall, and 5.93 $cm \cdot s^{-1}$ and 0.2 kg on the acrylic ceiling wall respectively, which could provide practical reference for the robot's application on multiple walls. However, although the robot can climb on a variety of wall surfaces, it is difficult for the robot to achieve wall tasks when the surface asperities vary greatly.

Acknowledgment

This work was supported by grants from Science and Technology Major Project of Anhui Province (17030901034), and Jiangsu Key Research and Development Plan (BE2017067).

References

[1] Liu Y W, Sun S M, Wu X, Mei T. A wheeled wall-climbing robot with bio-inspired spine mechanisms. *Journal of Bionic Engineering*, 2015, **12**, 17–28.

[2] Xu Z L, Ma P S. A wall-climbing robot for labeling scale of oil tank's volume. *Robotica*, 2002, **20**, 209–212.

[3] Choi H R, Ryew S M, Kang T H, Lee J H, Kim H M. A wall climbing robot with closed link mechanism. *Proceeding of International Conference on Intelligent Robotic Systems Conference*, Takamatsu, Japan, 2000, 2006–2011.

[4] Liu S L, Zhao Y Z, Gao X S, Xu D G, Wang Y. A wall climbing robot with magnetic crawlers for sand-blasting spray-painting and measurement. *High Technology Letters*, 2000, **9**, 86–88. (in Chinese)

[5] Schmidt D, Berns K. Climbing robots for maintenance and inspections of vertical structures – A survey of design aspects and technologies. *Robotics & Autonomous Systems*, 2013, **61**, 1288–1305.

[6] Chu B, Jung K, Han C S, Hong D. A survey of climbing robots: Locomotion and adhesion. *International Journal of Precision Engineering & Manufacturing*, 2010, **11**, 633–647.

[7] Grasso F W, Setlur P. Inspiration, simulation and design for smart robot manipulators from the sucker actuation mechanism of cephalopods. *Bioinspiration & Biomimetics*, 2007, **2**, 170–181.

[8] Zhu H F, Guan Y S, Wu W Q, Guan L M, Zhou X F, Zhang H. Autonomous pose detection and alignment of suction modules of a biped wall-climbing robot. *IEEE/ASME Transactions on Mechatronics*, 2015, **20**, 653–662.

[9] Li J, Gao X S, Fan N J, Li K J, Jiang Z H, Jiang Z J. Adsorption performance of sliding wall-climbing robot. *Chinese Journal of Mechanical Engineering*, 2010, **23**, 733–741.

[10] Zhou Q, Li X. Experimental investigation on climbing robot using rotation-flow adsorption unit. *Robotics & Autonomous Systems*, 2018, **105**, 112–120.

[11] Hillenbrand C, Schmidt D, Berns K. CROMSCI: Development of a climbing robot with negative pressure adhesion for inspections. *Industrial Robot*, 2008, **35**, 228–237.

[12] Zhao Y Z, Fu Z, Cao Q X, Wang Y. Development and applications of wall-climbing robots with a single suction cup. *Robotica*, 2004, **22**, 643–648.

[13] Illingworth L, Reinfeld D. *Vortex Attractor for Planar and Non-planar Surfaces*, US, US6619922, 2003.

[14] Asbeck A T, Kim S, McClung A, Parness A, Cutcosky M R. Climbing walls with microspines. *Proceeding of International Conference on Robotics and Automation*, Orlando, USA, 2006, 4315–4317.

[15] Kim S, Asbeck A T, Cutcosky M R, Provacher W R. Spinybot II: Climbing hard walls with compliant microspines. *Proceeding of International Conference on Advanced Robotics*, Seattle, USA, 2005, 601–606.

[16] Autumn K, Buehler M, Cutkosky M, Fearing R, Full R J, Goldman D, Groff R, Provancher W, Rizzi A A, Saranli U, Saunders A, Koditscheck D E. Robotics in scansorial environments. *Proceeding of Unmanned Ground Vehicle Technology VII. International Society for Optics and Photonics*, Bellingham, USA, 2005, 291–302.

[17] Haynes G C, Khripiny A, Lynch G, Amory J, Saunders A, Rizzi A A, Koditschek D E. Rapid pole climbing with a quadrupedal robot. *Proceeding of International Conference on Robotics and Automation*, Kobe, Japan, 2009, 2767–2772.

[18] Bartsch S, Birnschein T, Römmermann M, Hilljegerdes J, Kühn D, Kirchner F. Development of the six-legged walking and climbing robot space-climber. *Journal of Field Robotics*, 2012, **29**, 506–532.

[19] Chen D L, Zhang Q, Liu S Z. Design and realization of a flexible claw of rough wall climbing robot. *Advanced Materials Research*, 2011, **328**, 388–392.

[20] Burgard W, Brock O, Stachniss C. Design of a bioinspired dynamical vertical climbing robot. In: *Robotics*: *Science and Systems III*, MIT Press, Massachusetts, USA, 2008, 9–16.

[21] Parness A, McKenzie C. DROP: The durable reconnaissance and observation platform. *Industrial Robot*, 2013, **40**, 218–223.

[22] Tian Y, Tao D S, Pesika N, Wan J. Flexible control and coupling of adhesion and friction of gecko setal array during sliding. *Tribology Online*, 2015, **10**, 106–114.

[23] Yu Z W, Shi Y, Xie J X, Yang S X. Design and analysis of a bionic adhesive foot for gecko robot climbing the ceiling. *International Journal of Robotics and Automation*, 2018, **33**, 445–454.

[24] Unver O, Sitti M. Tankbot: A palm-size, tank-like climbing robot using soft elastomer adhesive treads. *The International Journal of Robotics Research*, 2010, **29**, 1761–1777.

[25] Seo T W, Sitti M. Tank-like module-based climbing robot using passive compliant joints. *IEEE/ASME Transactions on Mechatronics*, 2013, **18**, 397–408.

[26] Murphy M P, Kute C, Mengüç Y, Sitti M. Waalbot II: Adhesive recovery and improved performance of a climbing robot using fibrillar adhesives. *The International Journal of Robotics Research*, 2011, **30**, 118–133.

[27] Gorb S N. Uncovering insect stickiness: Structure and properties of hairy attachment devices. *American Entomologist*, 2005, **51**, 31–35.

[28] Ditsche P, Wainwright D K, Summers A P. Attachment to challenging substrates – Fouling, roughness and limits of adhesion in the northern clingfish (*Gobiesox maeandricus*). *Journal of Experimental Biology*, 2014, **217**, 2548–2554.